Combining Powder Bed Compaction and Nanopowders to Improve Density in Ceramic Binder Jetting Additive Manufacturing

Mohammadamin Moghadasi[a], Guanxiong Miao[b], Ming Li[c], Zhijian Pei[c], Chao Ma[a,b,c,d,*]

[a] Department of Materials Science and Engineering, Texas A&M University, TX, USA

[b] Department of Mechanical Engineering, Texas A&M University, TX, USA

[c] Department of Industrial and Systems Engineering, Texas A&M University, TX, USA

[d] Department of Engineering Technology and Industrial Distribution, Texas A&M University, TX, USA

[*]Corresponding author. E-mail address: cma@tamu.edu (Chao Ma)

Abstract

This paper reports a new approach to density improvement in ceramic binder jetting additive manufacturing: combining powder bed compaction and nanopowders. Samples were printed on a commercially available binder jetting 3D printer using an alumina nanopowder. Compaction thickness was varied across 0, 5, 10, 15, 20, and 60 μm at a layer thickness of 5 μm, and across 0, 100, and 200 μm at a layer thickness of 30 μm. Sintered density, as well as powder bed density, was measured. Furthermore, microstructure of sintered samples, with a focus on number and size of pores, was investigated to substantiate the density results. It was shown that at the same layer thickness, higher compaction thickness resulted in higher powder bed density, higher sintered density, and smaller number and size of pores in sintered samples. The highest sintered density (72.0%) achieved in this study was on par with the highest density reported in the literature on binder jetting of alumina without involving liquid feedstocks or special post-processing techniques (such as infiltration and isostatic pressing), demonstrating the effectiveness of this new approach to density improvement.

Keywords

Ceramics, binder jetting, additive manufacturing, density, powder bed compaction, nanopowders

1 Introduction

In recent decades, the advent of additive manufacturing (AM) provided new opportunities for producing ceramic parts [1–3]. AM is defined as a process of joining materials, usually layer by layer, following 3D model data. Binder jetting is among the seven main AM process categories

[4]. In binder jetting, a powder bed is first formed, and a liquid binding agent is then selectively deposited to join powder materials [4–7]. This printing step is repeated layer by layer to form a green part. The green part is then subjected to debinding and sintering. Advantages of binder jetting include low operating cost, no thermal residual stresses [8], no need of support structures for overhangs [9], high production rates [10], better powder recyclability [10], and most importantly, the capability of printing a variety of materials including ceramics [11]. In binder jetting, since the shaping (printing) step occurs at room temperature, typical manufacturing issues associated with ceramics (such as thermal residual stress and thermal shock failure) are avoided.

Advanced ceramic materials have exceptional properties, such as high hardness, high strength/weight ratio, high biocompatibility, and high wear, heat, and corrosion resistance [12,13]. Therefore, they play a vital role in various applications, such as hip joints replacements [14], high temperature engines [15], ballistic armor [16], chemical resistant impellers [16], and heat exchangers [17]. In most of these applications, the ceramic parts are subjected to high mechanical, tribological, thermal, or chemical loads. Thus, to fulfil the requirements for these applications, dense ceramic parts with proper material properties are required.

At present, low density of sintered parts remains an issue for binder jetting of ceramic materials. This low density issue and, as a result, inferior material properties have hindered the widespread industrial application of ceramic binder jetting [31]. Many approaches have been reported to improve density [18–30], and are covered in a recently published review paper focusing on density in binder jetting of ceramic materials [31]. The techniques to improve the part density can be classified into three categories: materials preparation (particle coating [18], powder granulation [19], mixing powders with different particle sizes [20,21], using slurry feedstock [22], etc.), printing (optimizing printing parameters [23], applying compaction [24–28], etc.), and post-processing (infiltration [29], isostatic pressing [30], etc.).

Du et al. [31] concluded that to obtain dense ceramic parts by binder jetting, using nanopowders is advantageous due to their high sinterability. Nevertheless, the usage of nanopowders is limited in binder jetting of ceramic materials due to their poor flowability. The poor flowability of nanopowders causes difficulties in powder spreading and thus results in low powder bed density [19,31–33]. For instance, in their study on binder jetting using an alumina nanopowder, Miao et al. achieved a low powder bed density of 6% and thus a low sintered density

of 32% [19]. Therefore, this low powder bed density issue needs to be addressed so that binder jetting can benefit from the high sinterability of nanopowders.

A few studies showed that powder bed compaction with a forward-rotating roller could improve powder bed density [25–28]. However, all of these studies were conducted on micropowders [25–28]. There are no reported studies on applying powder bed compaction to nanopowders. This study aims to fill this gap.

A binder jetting 3D printer (ExOne Innovent+) became commercially available recently. It allows for powder bed compaction with a forward-rotating roller. In this study, an alumina nanopowder is used on this printer and powder bed compaction is applied to increase powder bed density and thus sintered density. Experiments are performed at different values of compaction thickness and layer thickness.

2 Materials and Methods

2.1 Feedstock powder

The feedstock powder used for this study was a de-agglomerated alumina nanopowder (90-187195, Allied High Tech, CA, USA). The alumina nanopowder, used in the current study and the authors' previous paper [19], is the finest powder used in all reported studies on binder jetting thus far. The as-received nanopowder was examined with a scanning electron microscope (SEM, FERA-3, TESCAN, Czech Republic). SEM images of the as-received alumina nanopowder (Figure 1) show that the size of the nanoparticles was about 100 nm. Most of the nanoparticles slightly agglomerated and formed small clusters with irregular shapes.

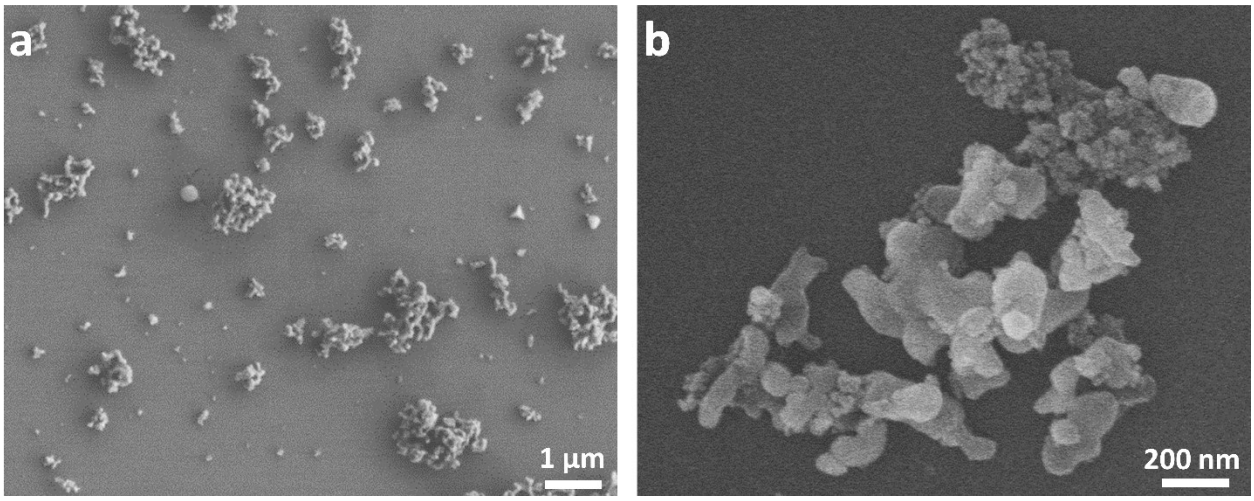

Figure 1. SEM images of the as-received alumina nanopowder. SEM parameters: beam accelerating voltages of a) 3.0 kV and b) 15.0 kV, and working distance of 8.0 mm.

Apparent density, tap density, Hausner ratio, Carr index, and repose angle were measured to evaluate the flowability of the alumina nanopowder. Their definitions are discussed elsewhere [31]. Their values are shown in the second column of Table 1. To compare the flowability of the alumina nanopowder with an alumina micropowder, the flowability measurements for an alumina micropowder with a particle size of 70 µm are shown in the last column of Table 1 [34]. All of these measurements indicate the alumina nanopowder has a significantly lower flowability than the alumina micropowder. Based on the values of Hausner ratio, Carr index, and repose angle, the flowability of the alumina nanopowder is classified as “very poor” [35–38].

Table 1. Flowability measurements for the as-received alumina nanopowder used in this study compared with an alumina micropowder in the literature [34].

Flowability metric	***Alumina nanopowder***	***Alumina micropowder*** [34]
Apparent density (%)	6.4 ± 0.0	52.6 ± 0.4
Tap density (%)	13.8 ± 0.2	59.8 ± 0.5
Hausner ratio	2.2 ± 0.8	1.1 ± 0.0
Carr index	53.8 ± 0.8	12.3 ± 0.1
Repose angle (°)	52.6 ± 2.1	25.3 ± 1.6

2.2 Printing process

A binder jetting 3D printer (Innovent+, ExOne company, North Huntington, PA, USA) and an aqueous binder (BA005, ExOne company, North Huntington, PA, USA) were used for printing samples. Figure 2 schematically shows the printing process in four steps for each layer. First, the build platform is lowered by the height of layer thickness (LT) plus compaction thickness (CT). The heat lamp moves over the build platform to dry the powder bed. Second, the hopper (that contains the feedstock powder) moves (from right to left) over the build platform and simultaneously deposits the powder. The roller spreads the powder (from right to left) with a counter rotating motion (clockwise rotation). Third, the spread powder layer with a height of LT plus CT is compacted to a height of LT through raising the build platform by the height of CT and then allowing the same roller to traverse on the powder layer with a forward-rotating motion. The compaction step is described in detail elsewhere [24]. Lastly, the print head moves over the powder bed and jets the binder onto selected areas, joining the powder according to the 3D model of the samples to be printed.

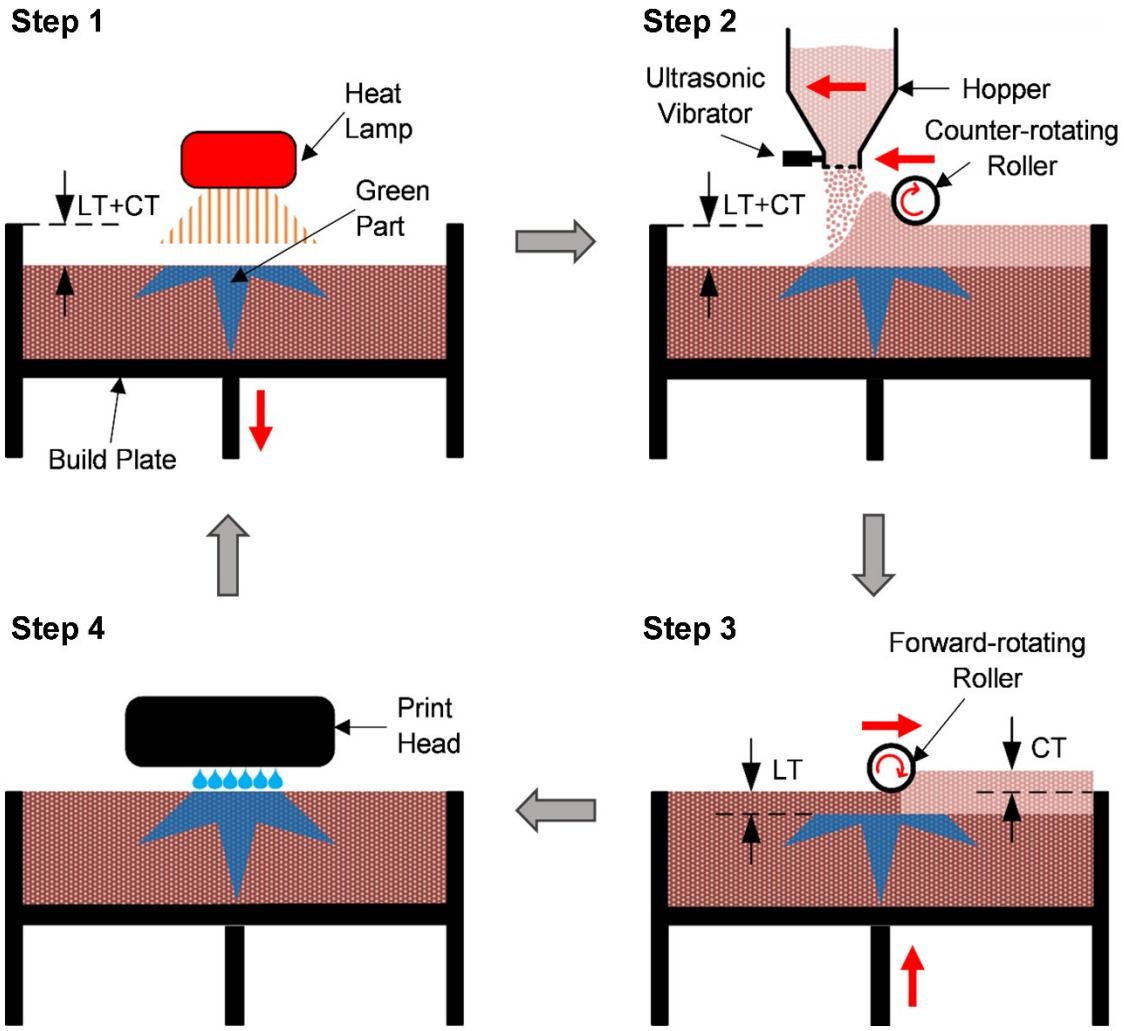

Figure 2. Four steps of the printing process with powder bed compaction (LT and CT mean layer thickness and compaction thickness, respectively).

In this study, compaction thickness and layer thickness were varied in nine prints in this study, as listed in Table 2. Table 3 shows the values of the parameters that were kept constant. These constant printing parameters were chosen by conducting preliminary trials and observing the dispensing, spreading, and printing qualities. The recoat speed determines the amount of powder deposited by the hopper (while traversing over the build platform as in Step 2 of Figure 2). The amount of powder needed for each layer changes if layer thickness or compaction thickness changes. Therefore, according to layer thickness and compaction thickness of each print, recoat speed was adjusted in the range of 30 to 60 mm/s. The roller traverse speed during compaction is the traverse speed of the roller as it moves across the build platform and compacts the additional

deposited powder into the powder bed. The binder set time is the time duration for which the binder is allowed to soak into the powder bed before drying/curing, and the bed temperature determines the temperature of the powder bed during printing. The rest of the printing parameters in Table 3 were defined elsewhere [23,39].

In each print listed in Table 2, five square prisms were printed. The length and width of samples were the same and equal to 10 mm, and the height of samples was 10 mm when a layer thickness of 30 µm was used, and 1 mm when a layer thickness of 5 µm was used. After each print, the whole build box (containing the build platform, loose powder, and printed samples) was taken out from the printer and placed in a furnace (DX402C, Yamato Scientific America, USA) to cure the printed samples at 200 ºC for 240 minutes.

Table 2. Varied printing parameters and their values.

Print	***Layer thickness (µm)***	***Compaction thickness (µm)***
1	5	0
2	5	5
3	5	10
4	5	15
5	5	20
6	5	60
7	30	0
8	30	100
9	30	200

Table 3. Constant printing parameters and their values.

Printing parameter	*Value*
Ultrasonic intensity (%)	100
Roller traverse speed during spreading (mm/s)	5
Roller rotation speed during spreading (rpm)	100
Roller traverse speed during compaction (mm/s)	3
Binder saturation (%)	100
Binder set time (s)	5
Bed temperature (◦C)	50
Drying time (s)	10

2.3 Powder bed density measurements

Since almost all aqueous binder evaporated during curing, the mass of binder in the green samples after curing was negligible compared to the mass of all powder on the build platform (including the green samples and loose powder). Thus, the mass of the green samples (m_{GS}) and the mass of loose powder (m_{LP}) on the build platform after curing were measured as the mass of the powder bed (m_{PB}). The depth of the powder bed (H_{PB}) for each print was measured by a caliper to calculate the volume of the powder bed (V_{PB}) given the area of the build platform (A_{PB}). By knowing the mass and the volume of the powder bed, powder bed density (ρ_{PB}) was calculated using Equation (1):

$$\rho_{PB} = \frac{m_{PB}}{V_{PB}} = \frac{m_{GS} + m_{LP}}{A_{PB} H_{PB}} \qquad (1)$$

2.4 Debinding and sintering processes

Debinding was performed to thermally decompose and burn out the binder. After debinding, sintering was performed to densify the samples. The green samples were placed in a furnace (KSL-1700X-A1-UL, MTI Corp., CA, USA) for debinding and sintering. The debinding and sintering profile is shown in Figure 3. First, the furnace was heated up to 470 °C with a heating rate of 2 °C/min and kept at 470 °C for 420 minutes for debinding. Then the furnace was heated

up to 1650 °C with a heating rate of 2 °C/min and kept at 1650 °C for 240 minutes for sintering. Finally, the samples were cooled down to room temperature in the furnace.

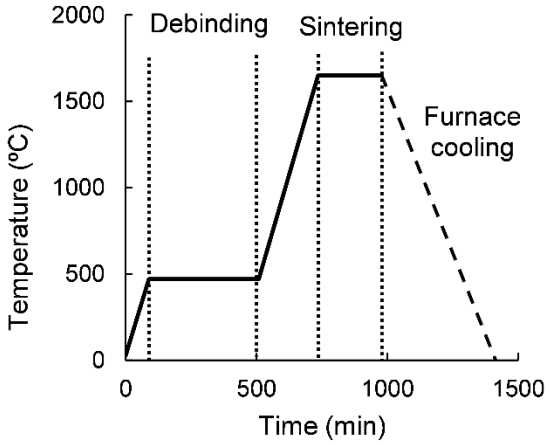

Figure 3. Temperature-time profile used during debinding and sintering.

2.5 Sintered density measurements

The Archimedes' method was used to measure bulk density of sintered samples by following the ISO 18754 standard [40]. Three samples from each print were used to measure the bulk density.

2.6 Characterization of microstructure

An optical microscope (OM, BX53, Olympus, Japan) was used to observe microstructure from the cross-sections of sintered samples. The cross-sections of sintered samples (perpendicular to the printing layers) were polished with 2000 grit SiC abrasive sandpaper and then were cleaned in an isopropanol solution for 20 minutes using an ultrasonic bath. In addition to OM, SEM was used to investigate the microstructure of sintered samples. The samples were manually broken by bending them with pliers along the build direction so that the fracture surfaces were parallel to the build direction. The SEM images were taken from the fracture surfaces of the samples.

3 Results and discussion

3.1 Effects of compaction on powder bed density

Figure 4 shows the effects of compaction thickness on powder bed density (at two different layer thickness values). Powder bed density of the alumina nanopowder without compaction is low

and greatly increases by applying powder bed compaction and increasing compaction thickness. The low powder bed density of the alumina nanopowder is probably due to the agglomeration of nanoparticles. Nanoparticles' tendency to agglomerate and form irregularly shaped clusters causes intra-clusters pores. These intra-clusters pores could result in low powder bed density. In addition to intra-clusters pores, the irregular shape of the clusters causes poor flowability, as indicated in Table 1. The poor flowability leads to formation of inter-cluster pores. But by applying compaction during printing, these clusters could be broken or rearrange, resulting in a more packed powder bed. Therefore, powder bed density increases by applying powder bed compaction during printing. This raising trend of powder bed density as a function of compaction thickness is consistent with reported studies on micropowders in the literature [25,27].

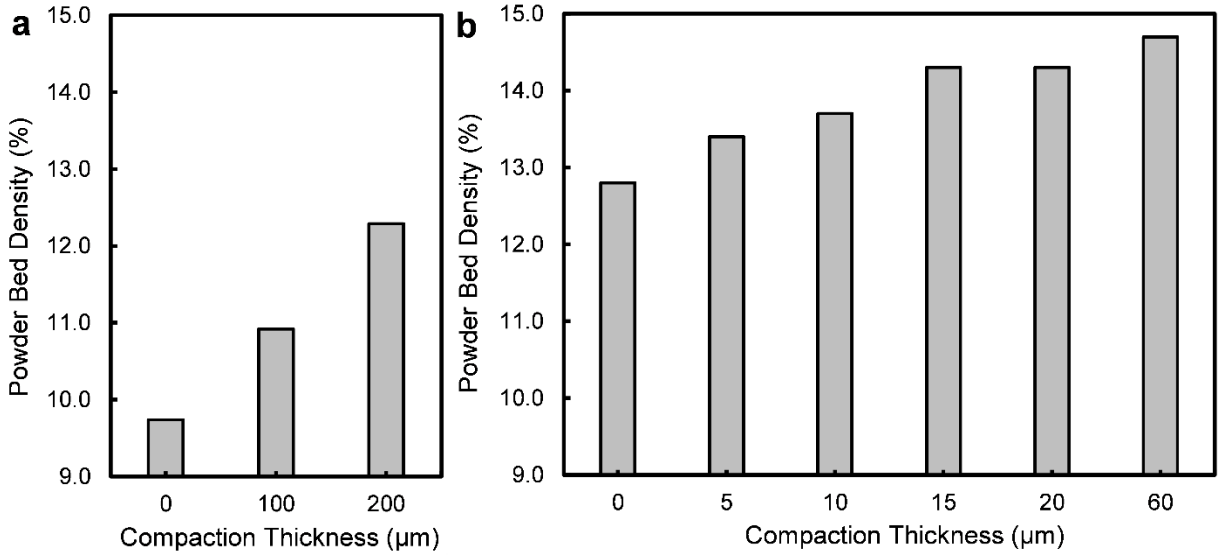

Figure 4. Effects of compaction thickness on powder bed density at a layer thickness of a) 30 µm and b) 5 µm.

Also worth mentioning is that powder bed density is not proportional to the compaction ratio (r_c) that is given by the following equation:

$$r_c = \frac{t_l + t_c}{t_l} \qquad (2)$$

where t_l and t_c are layer thickness and compaction thickness, respectively. A possible reason for this non-proportional relationship is the push-out phenomenon during the prints. During powder bed compaction, the roller pushes some powder out of the build envelope. Thus, not all powder is

compressed to the powder bed. Therefore, the proportional relationship between powder bed density and compaction ratio cannot hold.

3.2 Effects of compaction on sintered density

Figure 5 shows the effects of compaction thickness on bulk density of sintered samples. Similar to powder bed density, sintered density of samples increases as compaction thickness increases. The highest bulk density of 72.0% is accomplished at a layer thickness of 5 µm and a compaction thickness of 60 µm. In Figure 5, the error bars are standard deviations calculated from the three samples from each print.

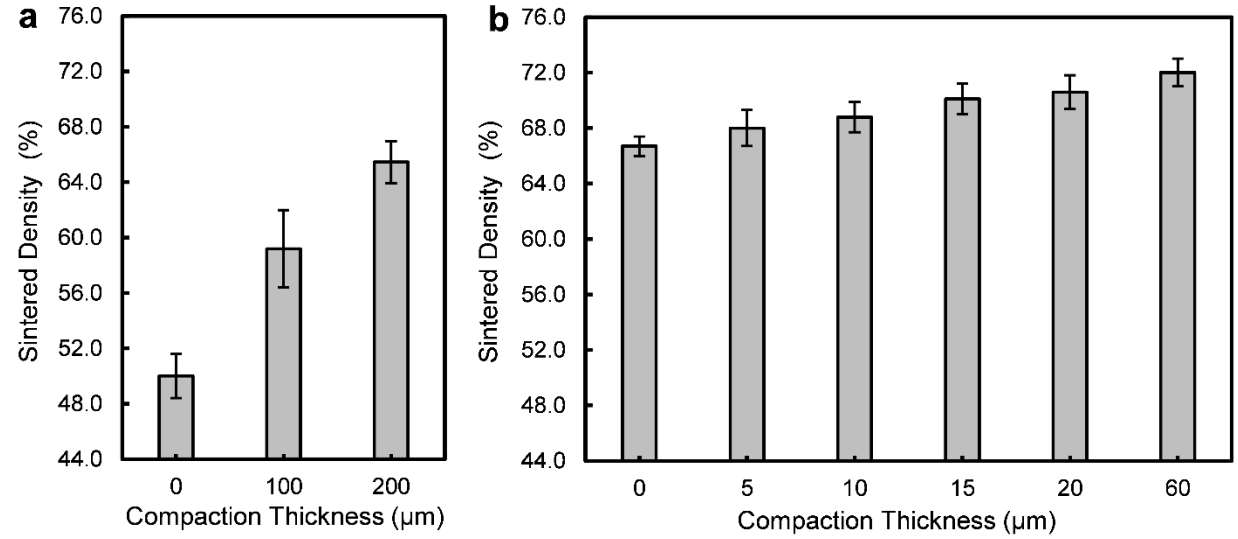

Figure 5. Effects of compaction thickness on bulk density of sintered samples at a layer thickness of (a) 30 µm and (b) 5 µm.

To compare the density results in this study with other reports, a literature search was conducted on binder jetting of alumina without involving unusual liquid feedstocks such as slurry [22] or special post-processing techniques such as infiltration [41] and isostatic pressing [28]. Figure 6 shows relative bulk density values of sintered alumina samples reported in the literature [19,21,28,31,42–44] in comparison with the current study. According to Figure 6, sintered density achieved in this study, 72.0%, is close to the highest one reported in the literature, 75.4% by Mariani et al. [44]. However, sintering was performed at a lower temperature in this study than in Mariani et al.'s study.

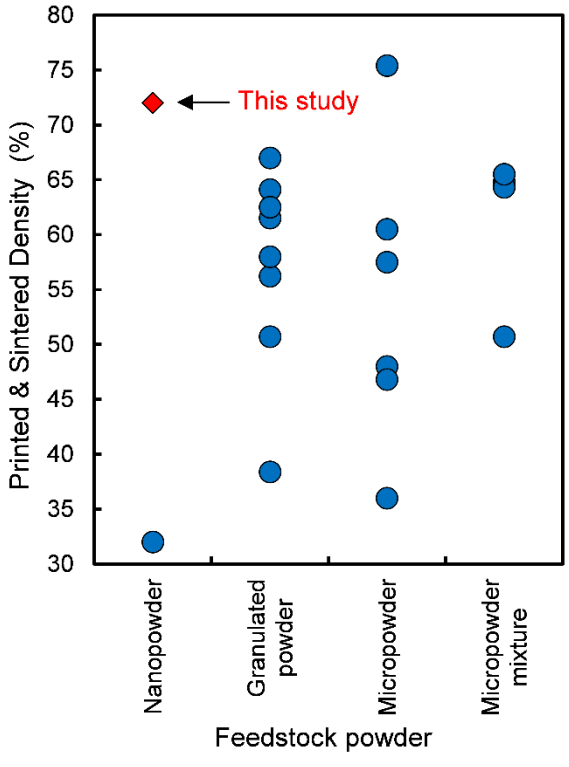

Figure 6. Sintered density of alumina samples with different feedstock powders in the literature [19,21,22,28,31,42–44] compared with this study.

3.3 Effects of compaction on microstructure of sintered samples

Figure 7 shows optical cross-section images from sintered samples without compaction and with the maximum compaction thickness tested in this study. The samples were prepared by grinding the samples along the build direction (perpendicular to the printing layers). These images show that there are no macroscopic voids or cracks in the structure of the samples. Pores were marked by red ellipses. A comparison of the number and size of the pores in Figure 7 shows that the fraction of pores in the structure reduces by applying powder bed compaction.

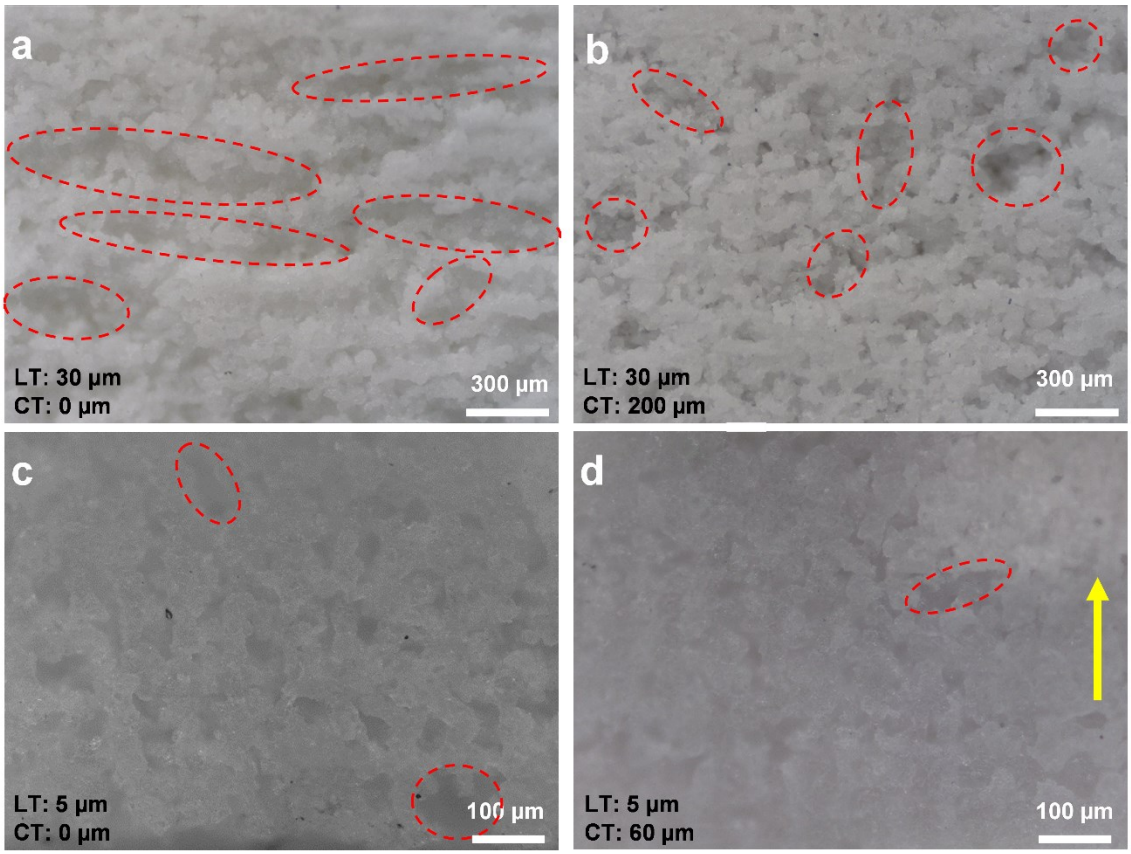

Figure 7. Optical images of ground cross-sections of sintered samples at different layer thickness (LT) and compaction thickness (CT) values: a) 30 µm and 0 µm, b) 30 µm and 200 µm, c) 5 µm and 0 µm, and d) 5 µm and 60 µm (the build direction is the same in all images and shown by the vertical yellow arrow, and the pores are indicated by the red ellipses).

Figure 8 shows SEM images of sintered samples without compaction and with the maximum compaction thickness tested in this study. By applying compaction, the number of large pores (indicated by horizontal red arrows) in the microstructure is decreased. Therefore, the OM and SEM images of the microstructure of the samples substantiate the density measurement results.

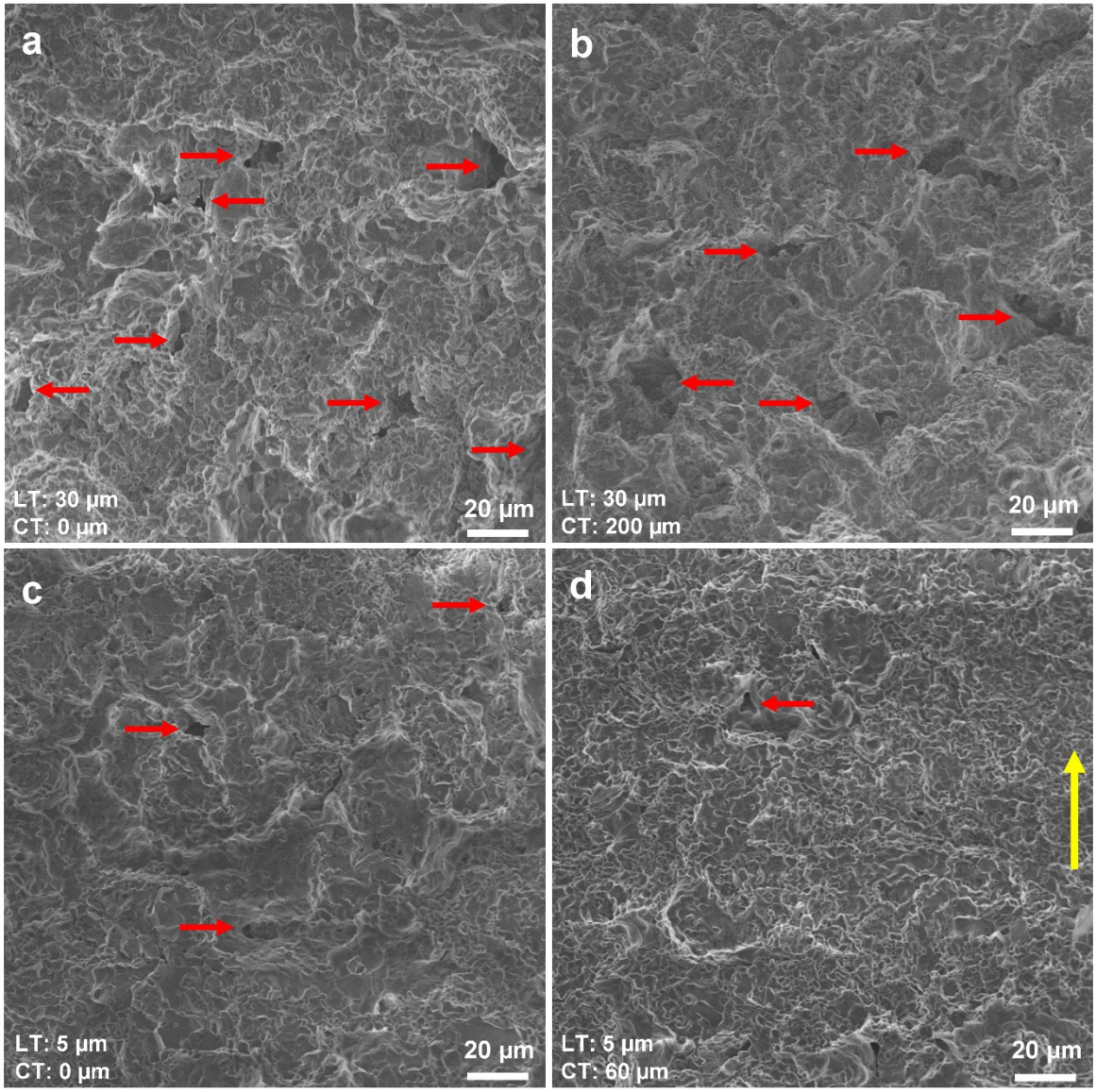

Figure 8. SEM images of fracture surfaces of sintered samples at different layer thickness (LT) and compaction thickness (CT) values: a) 30 µm and 0 µm, b) 30 µm and 200 µm, c) 5 µm and 0 µm, and d) 5 µm and 60 µm (the build direction is the same in all images and shown by the vertical yellow arrow, and the pores are indicated by the horizontal red arrows). SEM parameters: beam accelerating voltage of 5.0 kV and working distance of 14.7 mm.

Figure 9 shows high-magnification SEM images taken from the fracture surface of samples with the highest density (achieved by a layer thickness of 5 µm and a compaction thickness of 60 µm). As shown in Figure 9, a few fully dense areas could be observed in the microstructure of this sample. According to the approximate geometric changes associated with each stage of sintering [44], it could be inferred that these dense areas probably reached the final stage of sintering. These

types of microstructure are rarely observed in other samples of this study. Formation of these fully dense areas is probably due to powder bed compaction.

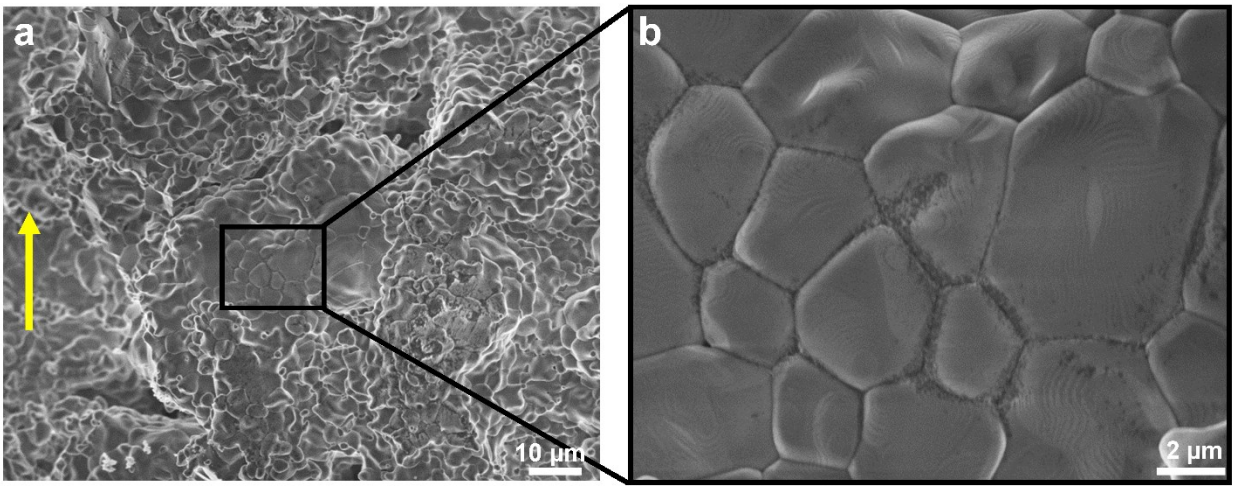

Figure 9. SEM images of the fracture surface of sintered sample with the highest bulk density achieved at a layer thickness of 5 µm and a compaction thickness of 60 µm (the build direction is shown by the vertical yellow arrow). SEM parameters: beam accelerating voltage of 5.0 kV and working distance of 15.0 mm.

4 Conclusions

A binder jetting machine was used to print alumina samples using a nanopowder with the assistance of powder bed compaction (through a forward-rotating roller). At the same layer thickness, increasing compaction thickness increased powder bed density as well as sintered density. Microstructure characterization showed that applying powder bed compaction decreased the number and size of pores in sintered samples. The highest bulk density achieved in this study was 72.0%. This bulk density value is on par with the highest density reported in the literature on binder jetting of alumina without involving liquid feedstock or special post-processing techniques such as infiltration and isostatic pressing. The main contribution of this paper is that it presents, for the first time, a new approach of using nanopowders and power bed compaction together to improve part density. Although the claim cannot be made that this approach will produce the highest density in resultant parts, this approach is a useful alternative to other reported approaches of improving density in ceramic binder jetting additive manufacturing.

Data availability

The raw data and the processed data required to reproduce these findings are available upon request from the corresponding author.

Acknowledgement

This material is based upon work partially supported by the National Science Foundation under Grant No. 2047908.

References

[1] A. Zocca, P. Colombo, C.M. Gomes, J. Günster, Additive manufacturing of ceramics: Issues, potentialities, and opportunities, J. Am. Ceram. Soc. 98 (2015) 1983–2001. https://doi.org/10.1111/jace.13700.

[2] J. Deckers, J. Vleugels, J.P. Kruth, A. Zocca, P. Colombo, C.M. Gomes, J. Günster, J. Deckers, J. Vleugels, J.P. Kruth, Additive manufacturing of ceramics: A review, J. Ceram. Sci. Technol. 5 (2014) 245–260. https://doi.org/10.4416/JCST2014-00032.

[3] L. Yang, H. Miyanaji, Ceramic additive manufacturing: A review of current status and challenges, in: 28th Annu. Int. Solid Free. Fabr. Symp., 2017.

[4] Standard terminology for additive manufacturing – General principles – Terminology, ASTM Int. i (2015) 1–9. https://doi.org/10.1520/F2792-12A.2.

[5] E.M. Sachs, J.S. Haggerty, M.J. Cima, P.A. Williams, Three-dimensional printing techniques, US Patent, No. 5204055, 1993.

[6] M. Moghadasi, W. Du, M. Li, Z. Pei, C. Ma, Ceramic binder jetting additive manufacturing: Effects of particle size on feedstock powder and final part properties, Ceram. Int. 46 (2020) 16966–16972. https://doi.org/10.1016/j.ceramint.2020.03.280.

[7] M. Li, W. Du, A. Elwany, Z. Pei, C. Ma, Metal Binder Jetting Additive Manufacturing: A Literature Review, J. Manuf. Sci. Eng. 142 (2020). https://doi.org/10.1115/1.4047430.

[8] A. Mostafaei, E.L. Stevens, J.J. Ference, D.E. Schmidt, M. Chmielus, Binder jet printing of partial denture metal framework from metal powder, in: Mater. Sci. Technol. Conf. Exhib. 2017, MS T 2017, Association for Iron and Steel Technology, AISTECH, 2017: pp. 289–

291. https://doi.org/10.7449/2017/MST_2017_289_291.

[9] M. Ziaee, N.B. Crane, Binder jetting: A review of process, materials, and methods, Addit. Manuf. 28 (2019) 781–801. https://doi.org/10.1016/j.addma.2019.05.031.

[10] A. Mostafaei, A.M. Elliott, J.E. Barnes, C.L. Cramer, P. Nandwana, M. Chmielus, Binder jet 3D printing – process parameters, materials, properties, and challenges, Prog. Mater. Sci. (2020) 100684. https://doi.org/10.1016/j.pmatsci.2020.100684.

[11] B. Utela, D. Storti, R. Anderson, M. Ganter, A review of process development steps for new material systems in three dimensional printing (3DP), J. Manuf. Process. 10 (2008) 96–104. https://doi.org/10.1016/j.jmapro.2009.03.002.

[12] N.P. Padture, Advanced structural ceramics in aerospace propulsion, Nat. Mater. 15 (2016) 804–809. https://doi.org/10.1038/nmat4687.

[13] J. Chevalier, L. Gremillard, Ceramics for medical applications: A picture for the next 20 years, J. Eur. Ceram. Soc. 29 (2009) 1245–1255. https://doi.org/10.1016/j.jeurceramsoc.2008.08.025.

[14] R. Sonntag, J. Reinders, J. Kretzer, What's next? Alternative materials for articulation in total joint replacement., Acta Biomater. 8 (2012) 2434–2441. https://doi.org/10.1016/J.ACTBIO.2012.03.029.

[15] A.S. Gohardani, O. Gohardani, Ceramic engine considerations for future aerospace propulsion, Aircr. Eng. Aerosp. Technol. 84 (2012) 75–86. https://doi.org/10.1108/00022661211207884.

[16] R.B. Heimann, Classic and Advanced Ceramics: From Fundamentals to Applications, Wiley-VCH, 2010. https://doi.org/10.1002/9783527630172.

[17] Q. Li, G. Flamant, X. Yuan, P. Neveu, L. Luo, Compact heat exchangers: A review and future applications for a new generation of high temperature solar receivers, Renew. Sustain. Energy Rev. 15 (2011) 4855–4875. https://doi.org/10.1016/J.RSER.2011.07.066.

[18] W. Du, X. Ren, C. Ma, Z. Pei, Ceramic binder jetting additive manufacturing: Particle coating for increasing powder sinterability and part strength, Mater. Lett. 234 (2019) 327–330. https://doi.org/10.1016/j.matlet.2018.09.118.

[19] G. Miao, W. Du, M. Moghadasi, Z. Pei, C. Ma, Ceramic binder jetting additive manufacturing: Effects of granulation on properties of feedstock powder and printed and sintered parts, Addit. Manuf. 36 (2020) 101542. https://doi.org/10.1016/j.addma.2020.101542.

[20] C. Sun, X. Tian, L. Wang, Y. Liu, C.M. Wirth, J. Günster, D. Li, Z. Jin, Effect of particle size gradation on the performance of glass-ceramic 3D printing process, Ceram. Int. 43 (2017) 578–584. https://doi.org/10.1016/J.CERAMINT.2016.09.197.

[21] W. Du, J. Roa, J. Hong, Y. Liu, Z. Pei, C. Ma, Binder Jetting Additive Manufacturing: Effect of Particle Size Distribution on Density, J. Manuf. Sci. Eng. 143 (2021). https://doi.org/10.1115/1.4050306.

[22] J.E. Grau, Fabrication of Engineered Ceramic Components by the Slurry-Based Three Dimensional Printing Process, Massachusetts Institute of Technology, 1998.

[23] E. Mendoza Jimenez, D. Ding, L. Su, A.R. Joshi, A. Singh, B. Reeja-Jayan, J. Beuth, Parametric analysis to quantify process input influence on the printed densities of binder jetted alumina ceramics, Addit. Manuf. 30 (2019) 100864. https://doi.org/10.1016/j.addma.2019.100864.

[24] M. Li, X. Wei, Z. Pei, C. Ma, Binder Jetting Additive Manufacturing: Observations of Compaction-induced Powder Bed Surface Defects, Manuf. Lett. 28 (2021) 50–53. https://doi.org/10.1016/j.mfglet.2021.04.003.

[25] M. Ziaee, R. Hershman, A. Mahmood, N.B. Crane, Fabrication of demineralized bone matrix/polycaprolactone composites using large area projection sintering (LAPS), J. Manuf. Mater. Process. 3 (2019). https://doi.org/10.3390/jmmp3020030.

[26] T. Niino, K. Sato, Effect of powder compaction in plastic laser sintering fabrication, Solid Free. Fabr. Symp. 293 (2009) 205.

[27] J. Yoo, Fabrication and microstructural control of advanced ceramic components by three dimensional printing, Massachusetts Institute of Technology, 1996.

[28] J. Yoo, M.J. Cima, S. Khanuja, E.M. Sachs, J. Yoo, S. Khanuja, M. Rynerson, M. Rynerson, D. Nammour, B. Giritlioglu, J. Grau, E.M. Sachs, M.J. Cima, S. Khanuja, E.M. Sachs, Structural ceramic components by 3D printing, Solid Free. Fabr. Symp. (1993) 40–50.

http://hdl.handle.net/2152/65035.

[29] W. Zhang, R. Melcher, N. Travitzky, R.K. Bordia, P. Greil, Three-Dimensional Printing of Complex-Shaped Alumina/Glass Composites, Adv. Eng. Mater. 11 (2009) 1039–1043. https://doi.org/10.1002/ADEM.200900213.

[30] C.A. Díaz-Moreno, Y. Lin, A. Hurtado-Macías, D. Espalin, C.A. Terrazas, L.E. Murr, R.B. Wicker, Binder jetting additive manufacturing of aluminum nitride components, Ceram. Int. 45 (2019) 13620–13627. https://doi.org/10.1016/J.CERAMINT.2019.03.187.

[31] W. Du, X. Ren, Z. Pei, C. Ma, Ceramic binder jetting additive manufacturing: A literature review on density, J. Manuf. Sci. Eng. 142 (2020) 1–66. https://doi.org/10.1115/1.4046248.

[32] W. Du, X. Ren, C. Ma, Z. Pei, Binder jetting additive manufacturing of ceramics: A literature review, in: ASME Int. Mech. Eng. Congr. Expo. Proc., 2017: pp. 1–12. https://doi.org/10.1115/IMECE2017-70344.

[33] M. Li, G. Miao, M. Moghadasi, Z. Pei, C. Ma, Ceramic Binder Jetting Additive Manufacturing: Relationships among Powder Properties, Feed Region Density, and Powder Bed Density, Ceram. Int. (2021). https://doi.org/10.1016/j.ceramint.2021.05.175.

[34] W. Du, G. Miao, L. Liu, Z. Pei, C. Ma, Binder jetting additive manufacturing of ceramics: Comparison of flowability and sinterability between raw and granulated powders, in: ASME 2019 14th Int. Manuf. Sci. Eng. Conf., American Society of Mechanical Engineers (ASME), 2019: pp. 1–8. https://doi.org/10.1115/MSEC2019-2983.

[35] H. Hausner, Friction conditions in a mass of metal powder, Int. J. Powder Met. 3 (1967) 7–13.

[36] R.L. Carr, Evaluating Flow Properties of Solids, Chem. Eng. 18 (1965) 163–168.

[37] R.B. Shah, M.A. Tawakkul, M.A. Khan, Comparative evaluation of flow for pharmaceutical powders and granules, AAPS PharmSciTech. 9 (2008) 250–258. https://doi.org/10.1208/s12249-008-9046-8.

[38] M.A. Kaleem, M.Z. Alam, M. Khan, S.H.I. Jaffery, B. Rashid, An experimental investigation on accuracy of Hausner Ratio and Carr Index of powders in additive manufacturing processes, Met. Powder Rep. (2020).

https://doi.org/10.1016/j.mprp.2020.06.061.

[39] H. Miyanaji, K.M. Rahman, M. Da, C.B. Williams, Effect of fine powder particles on quality of binder jetting parts, Addit. Manuf. 36 (2020) 101587. https://doi.org/10.1016/j.addma.2020.101587.

[40] ISO, Fine Ceramics (Advanced Ceramics, Advanced Technical Ceramics)-Determination of Density and Apparent Porosity porosity, ISO 18754. (2003).

[41] R. Melcher, S. Martins, N. Travitzky, P. Greil, Fabrication of Al_2O_3-based composites by indirect 3D-printing, Mater. Lett. 60 (2006) 572–575. https://doi.org/10.1016/j.matlet.2005.09.059.

[42] R. Melcher, N. Travitzky, C. Zollfrank, P. Greil, 3D printing of Al_2O_3/Cu-O interpenetrating phase composite, J. Mater. Sci. 46 (2011) 1203–1210. https://doi.org/10.1007/s10853-010-4896-3.

[43] S. Maleksaeedi, H. Eng, F.E. Wiria, T.M.H. Ha, Z. He, Property enhancement of 3D-printed alumina ceramics using vacuum infiltration, J. Mater. Process. Technol. 214 (2014) 1301–1306. https://doi.org/10.1016/j.jmatprotec.2014.01.019.

[44] M. Mariani, R. Beltrami, P. Brusa, C. Galassi, R. Ardito, N. Lecis, 3D printing of fine alumina powders by binder jetting, J. Eur. Ceram. Soc. (2021). https://doi.org/10.1016/j.jeurceramsoc.2021.04.006.